Semmling, M., Beckheinrich, J., Wickert, J., Beyerle, G., Schön, S., Fabra, F., Pflug, H., He, K., Schwabe, J., Scheinert, M. (2014): Sea surface topography retrieved from GNSS reflectometry phase data of the GEOHALO flight mission. - *Geophysical Research Letters*, *41*, 3, p. 954-960.

DOI: http://doi.org/10.1002/2013GL058725

AGU PUBLICATIONS

Geophysical Research Letters

RESEARCH LETTER
10.1002/2013GL058725

Key Points:
- Altimetric retrieval depicts geoid undulations of the Mediterranean Sea
- Residuals resolve the sea surface topography with centimeter precision
- Synergies with other techniques (radar altimeter) arise

Correspondence to:
A. M. Semmling,
maxsem@gfz-potsdam.de

Citation:
Semmling, A. M., J. Beckheinrich, J. Wickert, G. Beyerle, S. Schön, F. Fabra, H. Pflug, K. He, J. Schwabe, and M. Scheinert (2014), Sea surface topography retrieved from GNSS reflectometry phase data of the GEOHALO flight mission, *Geophys. Res. Lett.*, *41*, 954–960, doi:10.1002/2013GL058725.

Received 18 NOV 2013
Accepted 14 JAN 2014
Accepted article online 16 JAN 2014
Published online 11 FEB 2014

Sea surface topography retrieved from GNSS reflectometry phase data of the GEOHALO flight mission

A. M. Semmling[1], J. Beckheinrich[1], J. Wickert[1], G. Beyerle[1], S. Schön[2], F. Fabra[3], H. Pflug[1], K. He[1], J. Schwabe[4], and M. Scheinert[4]

[1]Department of Geodesy and Remote Sensing, Deutsches GeoForschungsZentrum, Potsdam, Germany, [2]Institut für Erdmessung, Leibniz Universität Hannover, Hannover, Germany, [3]Earth Observation Department, Institut d'Estudis Espacials de Catalunya (ICE/CSIC), Bellaterra, Spain, [4]Institut für Planetare Geodäsie, Technische Universität Dresden, Dresden, Germany

Abstract Sea surface topography observations are deduced from an airborne reflectometry experiment. A GNSS (Global Navigation Satellite System) receiver dedicated for reflectometry was set up aboard the German HALO (High Altitude Long Range) research aircraft. Flights were conducted over the Mediterranean Sea about 3500 m above sea level. A signal path model divided into large- and small-scale contributions is used for phase altimetry. The results depict geoid undulations and resolve anomalies of the sea surface topography. For the whole experiment 65 tracks over the Mediterranean Sea are retrieved and compared with a topography model. Tracks differ between right-handed and left-handed circular polarization. The difference, however, is not significant for this study. Precision and spatial resolution decrease disproportionately at low elevations. Eight tracks with centimeter precision are obtained between 11° and 33° of elevation. At higher elevation angles the number of tracks is significantly reduced due to surface roughness. In future such retrievals could contribute to ocean eddy detection.

1. Introduction

Observations of the sea surface topography are crucial to understand ocean eddies as an important climate indicator [*Fu et al.*, 2010] or contribute to tsunami detection [*Ablain et al.*, 2006]. The spatiotemporal resolution of current topographic observations is limited due to the rather sparse sampling of today's radar altimeters.

The Earth's gravity field essentially influences the sea surface and the distribution of water masses. Existing global gravity field models, e.g., EIGEN-6C2 [*Förste et al.*, 2011] or EGM-2008 [*Pavlis et al.*, 2012], provide a close-by equipotential surface: the geoid. The sea surface topography T is defined by deviations of the sea surface from the geoid (EIGEN-6C2), whereas the sea surface height H is defined above the ellipsoid (WGS-84) and includes geoid undulations. Models of the mean sea surface (MSS) approximate H globally [*Andersen and Knudsen*, 2009] providing a 1 arc min spatial resolution, e.g., DTU-10. A model of the mean ocean dynamic topography (MDT) is deduced from the difference between MSS and geoid.

Observations of the dynamic topography to resolve mesoscale ocean eddies are currently limited by the 10 day sampling and 70 km cross-track spacing of radar altimeter observations [*Bosch et al.*, 2012]. An improved sampling with multiple simultaneous tracks could be achieved using ocean reflections of GNSS (Global Navigation Satellite System) signals, as it has been proposed by *Martin-Neira* [1993]. In order to detect the dynamic topography such tracks need centimeter precision which is a challenging requirement for GNSS reflections (GNSS-R). Previous airborne studies on GNSS-R altimetry concentrated on code observations [*Lowe et al.*, 2002; *Ruffini et al.*, 2004; *Rius et al.*, 2010] or on Doppler observations [*Semmling et al.*, 2013]. This paper aims for observations of the sea surface topography using carrier phase data. Such data is difficult to retrieve due to incoherence introduced by rough surface scattering [*Beckmann and Spizzichino*, 1987], but it provides the highest precision in GNSS [*Misra and Enge*, 2001]. Based on a path model assuming specular reflection, residual phase tracks are retrieved and compared with predictions of MSS and MDT. Diffuse sea surface reflections are disregarded.

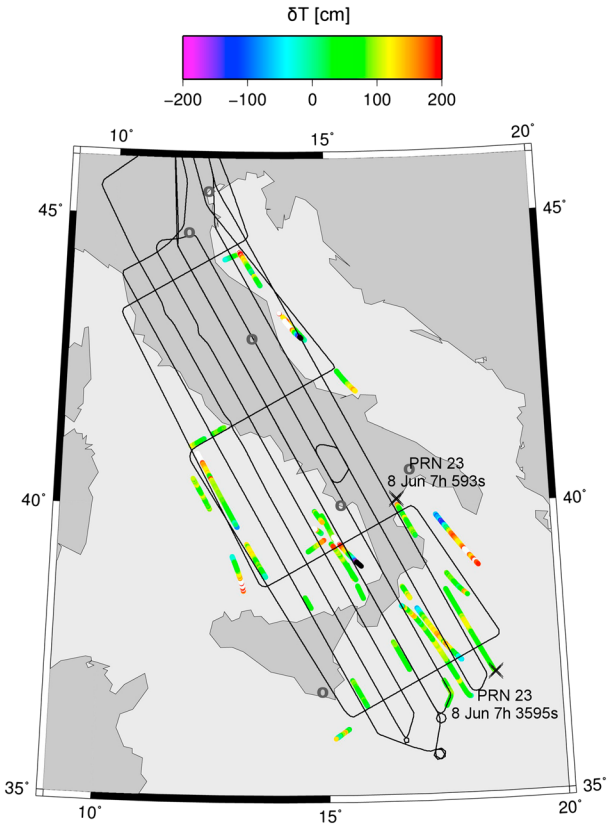

Figure 1. Flights of the GEOHALO mission. Transects are indicated by thin black lines. Gray circles mark GNSS reference stations used for trajectory calculation; six further stations lie outside this map. All retrieved tracks are added with the color-coded difference δT. Cross markers indicate start and end of the example event (PRN 23).

The remainder of the paper is structured as follows. The second section describes the flight experiment and the applied method. In the third section, altimetric results of the experiment are discussed, before the last section concludes this study.

2. Experiment and Method

The HALO research aircraft is dedicated to long-range flights at high altitudes for atmospheric and geophysical research [*Schlager et al.*, 2013]. Within the GEOHALO mission it provides a platform for GNSS-R observations and other measurements in the field of gravimetry, magnetometry, laser altimetry, and GNSS positioning [*Scheinert*, 2013; *Heyde et al.*, 2013]. Four mission flights were conducted (6, 8, 11, and 12 Jun 2012) with transects over Italy and adjacent parts of the Mediterranean Sea (thin black lines in Figure 1).

Three geodetic GNSS receivers were set up aboard the aircraft for navigation. A GPS flight trajectory has been calculated in postprocessing according to *Wang et al.* [2010]. A double-difference algorithm is used implementing multireference stations to improve the long-baseline precision [*Blewitt*, 1989].

A GORS type (GNSS Occultation Reflectometry Scatterometry) quad front end receiver was set up aboard for phase altimetry. Details on GORS receiver sampling with a similar airborne setup are described in *Semmling et al.* [2013]. Samples of GPS C/A (coarse acquisition) code signals are analyzed that have been acquired with GPS low-gain patch antennas (4.7 dBic max. gain, 114° 3 dB beam width). An up-looking antenna on top of the fuselage and two portside-looking antennas in a window viewport were installed (aircraft scheme in Figure 2). The portside antennas with right-handed circular polarization (RHCP) and left-handed circular polarization (LHCP) are dedicated to record reflection events at elevation angles between 3° and 90°. The seawater reflected power is dominated by LHCP(RHCP) above(below) the *Brewster* angle at 8° of elevation [*Smyrnaios et al.*, 2013]. Therefore, both polarizations are used to increase the detection probability. Polarization-related effects on phase observations are disregarded. Reflection events are recorded by the receiver when satellites are visible portside in the given elevation range. In this section the method is described analyzing an example event of the satellite with PRN (pseudorandom noise number) 23 indicated by cross markers in Figure 1.

2.1. Signal Path Model

Two quantities are distinguished. The phase observation ϕ defined by the phase angle in the range $[0, 2\pi)$ and the model p of the observed path in meter that is not confined to a specific range. The path modeled in a reflection event accounts for optical path lengths between transmitter X, receiver R, and specular reflection point S. The use of different antennas requires a baseline correction of p. Figure 2 shows important parameters of the path model.

The path p is calculated in a so-called Earth-fixed curvature-centered frame. The frame's principal feature is a sphere that locally approximates the Earth's curvature described by the WGS-84 ellipsoid [*Semmling*, 2012]. In this airborne experiment, the model p requires precise heights of the receiver aircraft A and the reflecting

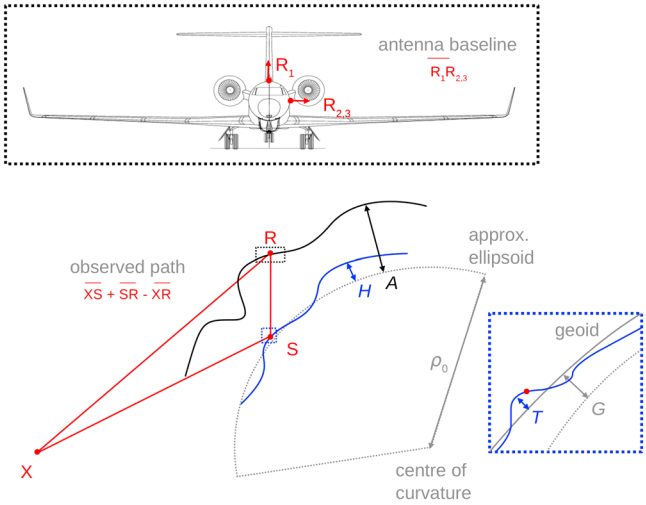

Figure 2. Scheme of the reflection model in a curvature-centered frame (not to scale). The model computes the observed path between the receiver (*R*), the transmitter (*X*), and the specular surface point (*S*). Ellipsoidal heights *A* and *H* correspond to spherical orbits $\rho_0 + A$ and $\rho_0 + H$ in the curvature-centered frame. A zoom on the sea surface (blue frame) shows that *H* splits into the geoid undulation *G* and the topography *T*. A zoom on the HALO aircraft (black frame) shows the different antenna positions: R_1 up-looking and $R_{2,3}$ portside-looking. Arrows indicate antenna orientations. The baseline (1.54 m long) is determined with centimeter accuracy in an aircraft body frame for model path correction.

surface *H*. Predictions of *H* and *A* for the example event are shown in Figure 3. For the following method these heights are split: $A = A_0 + \Delta A$ and $H = G + T$. By definition A_0 (the event's initial aircraft height) and *G* (the geoid undulation from EIGEN-6C2) denote large-scale components, whereas ΔA (the aircraft height variation) and *T* (the sea surface topography) are small-scale components.

Based on this splitting the path is approximated as follows:

$$p(A, H) \approx p(A_0, G) + p_A \, \Delta A + p_H \, T. \tag{1}$$

The large-scale term $p(A_0, G)$ requires ray tracing and is calculated with a coarse temporal resolution (10 s) for computational convenience. Details on this ray tracing, especially the tropospheric refraction model, are described in *Semmling et al.* [2012]. For the small-scale terms only the first order in ΔA and *T* is considered. The ray tracing provides height coefficients $p_A = [p(A_0 + \Delta, G) - p(A_0, G)]/\Delta$ and $p_H = [p(A_0, G + \Delta) - p(A_0, G)]/\Delta$ where Δ denotes a 1 m height offset. Approximations $p_A \approx 2 \sin E$

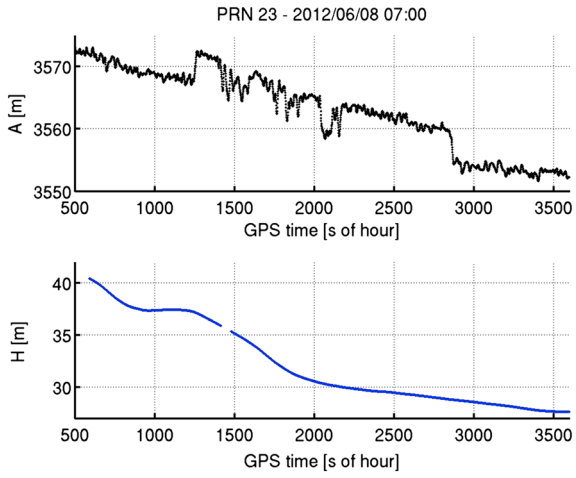

Figure 3. Height predictions for the example event (PRN 23). (top) Receiver height (black) based on aircraft trajectory. (bottom) Sea surface height (blue) based on MSS (DTU-10). The gap in sea surface height at about 1400 s indicates land reflections. The trend in both heights is similar as for navigation a constant aircraft altitude is set that refers to sea level. Land reflections before 500 s and during the gap at about 1400 s are excluded.

Table 1. Model Path Characteristics for the Example Event[a]

E	(deg)	25.8	… 11.6
$p(A,H)$	(m)	3069	… 1399
$p_A\,\Delta A$	(m)	−2.7	… −8.8
$p_H\,T$	(cm)	76	… 31
$\lvert p_H\rvert$		0.87	… 0.40
$\Delta p(\chi)$	(m)	0.4	… 0.9
$\Delta p(R_1,R_{2,3})$	(m)	−1.0	… −0.5
$2\,a$	(km)	0.2	… 0.6

[a]The rows contain (1) sat. elevation, (2) total path, (3) contributions of aircraft height variation, (4) contribution of sea surface topography, (5) height sensitivity, (6) water vapor correction, (7) antenna baseline correction, and (8) reflection footprint size.

and $p_H \approx -2 \sin E$, where E denotes the satellite elevation seen from the specular point, hold as long as ΔA and T are less than 10 m. For complete path modeling ΔA is taken with best resolution (0.1 s) from the GPS aircraft trajectory. Predictions of T are provided by the MDT model (DTU-10). Table 1 provides model path characteristics for the example event.

The path decreases significantly between the initial and the final elevation of the setting satellite. The magnitude $|p_H|$ describes the path's sensitivity to the surface height. It decreases with the elevation angle from about 87% to 40%. Contributions from aircraft height variation are in the meter range. Topography contributions are in the submeter range. Furthermore, corrections of antenna baselines $\Delta p(R_1, R_{2,3})$ and water vapor variations $\Delta p(\chi)$ are in a relevant range and have to be considered. Another important parameter of phase observations is the size of the reflection footprint given by the major axis $2\,a$ of the first *Fresnel* zone. It is calculated following a description of *Fresnel* zones for very different antenna heights in *Beckmann and Spizzichino* [1987]. Values for the example event are added in Table 1.

2.2. Surface Height Retrieval

The surface height is retrieved starting with a reduction of phase observation. A model path $p(A, G) = p(A_0, G) + p_A\,\Delta A$ is calculated including the large-scale term and small-scale aircraft contributions. This model is used to reduce phase observations for a facilitated retrieval. Following *Semmling et al.* [2013] filtered observations γ_{flt} are constructed from I, Q samples of the GORS receiver. The reduction of γ_{flt} using the model $p(A, G)$ provides a residual γ_0. A running mean filter with a 10 s window is applied to smooth out high-frequency noise. The smoothed residual γ_0 corresponds to the residual phase $\Delta\phi = \arg[\gamma_0]$. The phase $\Delta\phi$ is unwrapped, and a maximum phase gradient algorithm [*Ghiglia and Pritt*, 1998] is used to obtain continuous phase tracks (in cycles) within each event.

After the described reduction with the model path $p(A, G)$ particularly the topography term remains in the equation of observation:

$$\Delta\phi = \frac{1}{\lambda} p_H \cdot T + \nu. \tag{2}$$

The L band carrier wavelength is denoted λ. Also a bias term $\nu := \Delta n + \epsilon/\lambda$ remains as the phase ambiguity Δn and the path delay ϵ (induced by different lengths of antenna cables) are unknown.

Continuous phase tracks $\Delta\phi$, plotted with gray markers in Figure 4 (top), agree with the evolution of the MDT based model (blue lines). The bias ν results in a specific offset for each track.

Five tracks with elevations between 11° and 25° are distinguished for this event (Table 2): three (A, B, C) for RHCP data and two (b, c) for LHCP data. Continuous tracks cover time intervals of 7 to 11 min and extend on the surface over 55 to 83 km. Gaps of incoherence, particularly from 1200 s to 2100 s and at about 2800 s, coincide with abrupt changes in aircraft height data by several meters, cf. Figure 3 (top) indicating the influence of A and its uncertainty.

According to equation (2) residuals $\Delta\phi$ are used to retrieve the topography $T = \lambda\,\Delta\phi/p_H$ with an undetermined bias $\Delta T = \lambda\nu/p_H$ still persisting. The surface height is then composed $H = G + T + \Delta T$ where G refers to the geoid undulation (EIGEN-6C2).

3. Altimetric Results and Discussion

Figure 4 (middle and bottom) shows tracks of the topography T and the surface height H for the example event (above the geoid EIGEN-6C2 and the ellipsoid WGS-84, respectively). Figure 4 (bottom) depicts the agreement of height tracks with the MSS dominated by geoid undulations. Figure 4 (middle) shows topography tracks compared to the MDT. To quantify the topographic agreement the difference $\delta T := T - \text{MDT}$ is defined. The corresponding standard deviation δT_{std} provides a precision estimate along the track.

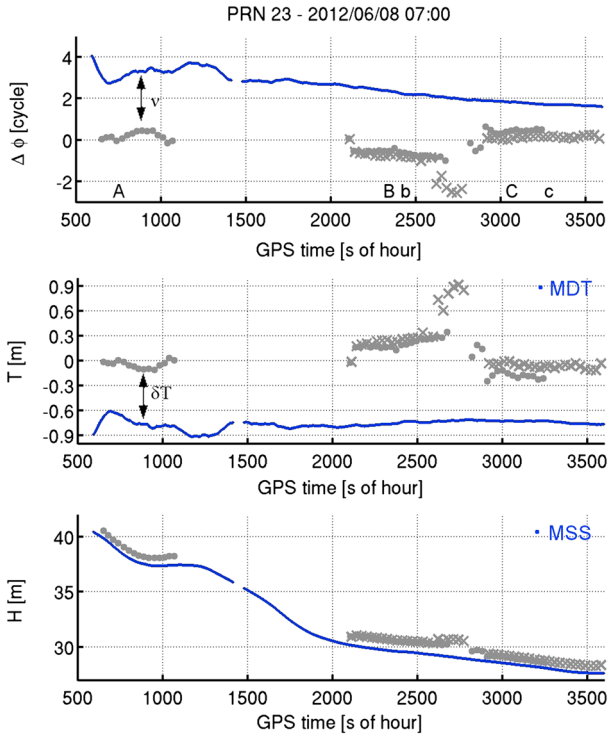

Figure 4. Phase residuals and surface height tracks are plotted versus GPS time for the example event considering RHCP data (dots) and LHCP data (crosses). (top) Residual phase tracks. (middle) Topography tracks above EIGEN-6C2 geoid. (bottom) Height tracks above WGS-84 ellipsoid. Model predictions (blue lines) based on MDT and MSS are plotted for comparsion.

Anomalies of the MDT (e.g., 15 cm peak to peak in track A) are resolved with centimeter precision ($\delta T_{\text{std}} = 4$ cm in track A). However, anomalies remain that cannot be explained by the MDT (e.g., in track b). Offsets in δT are related to the bias ΔT. Especially at low elevations where the sensitivity $|p_H|$ is small the bias ΔT becomes critical.

Further contributions to δT are expected due to uncertainties of the aircraft height A and the atmospheric water vapor χ. An instrumental uncertainty of A is given by the root-mean-square deviation $\delta A_{\text{rms}} < 10$ cm of two GNSS-based trajectories that are calculated with the same double difference algorithm for the same antenna using data of two different receivers. In order to better assess the uncertainty of A and its consequences for continuous phase retrievals a GNSS-independent trajectory would be required (but is not available for this study). The relative uncertainty of used water vapor profiles is about 10%. A critical topography bias (> 10 cm) induced by water vapor is expected at elevation angles below 10°.

Table 2. Track Parameters for the Example Event[a]

		A	B	b	C	c
t_0	(s)	650	2105	2112	2823	2920
Δt	(s)	446	585	680	448	677
Δs	(km)	55	70	82	55	83
$\overline{\delta T}$	(m)	0.7	1.0	1.1	0.6	0.7
δT_{std}	(cm)	4	5	25	13	4
E_{min}	(deg)	23.2	15.6	15.1	13.0	11.6
E_{max}	(deg)	25.5	18.3	18.2	15.0	14.6

[a]The different tracks are labeled with capital or small letters for RHCP/LHCP, respectively. The rows contain (1) GPS time start epoch in seconds of hour, (2) time interval, (3) track length, (4) mean topography difference, (5) precision estimate, (6/7) min./max. sat. elevation.

For the entire GEOHALO mission 65 continuous phase tracks are retrieved and plotted in Figure 1 with differences δT indicated. A 3 min threshold is set, i.e., tracks shorter than 3 min are not regarded. Centimeter precision ($\delta T_{\text{std}} < 10$ cm) is reported for eight tracks (12%) with elevation angles between 11° and 33°. Statistics for the tracks in different elevation classes are provided in Table 3.

Results for RHCP, LHCP show only small differences: for both polarizations the majority (80%, 83%) occurs below 15°, only a minority (20%,17%) occurs above. For slant tracks above 15°, however, the average precision and sensitivity are the highest. An average length

Table 3. Track Statistics Classified by Min. Elevation [a]

		$3° < E_{min} < 5°$		$5° < E_{min} < 15°$		$15° < E_{min} < 90°$	
		RHCP	LHCP	RHCP	LHCP	RHCP	LHCP
#	(tracks)	13	13	15	12	7	5
$\langle \Delta t \rangle$	(s)	410	392	433	482	351	381
$\langle \Delta s \rangle$	(km)	54	51	55	59	42	45
$\langle \delta T_{std} \rangle$	(cm)	84	85	45	33	11	12
$\langle 2\, a_{max} \rangle$	(km)	3.8	3.8	1.0	1.0	0.2	0.2
$\langle \lvert p_H \rvert \rangle$		0.2	0.2	0.4	0.4	0.7	0.9

[a]Each class differs between RHCP and LHCP. The rows contain (1) number of tracks and average values of (2) time interval, (3) track length, (4) precision estimate, (5) max. footprint size, and (6) mean height sensitivity.

greater than 40 km for all classes is achieved by the 3 min track threshold. LHCP tracks in average are slightly longer above 5° elevation.

Phase tracks prove a sensitivity to changes of the surface height H at the specular reflection point. However, certain limits have to be discussed. Due to low-pass filtering the retrieval is insensitive to along-track changes of H with wavelengths shorter than 1 km (e.g., wind waves). The sensitivity for long wavelengths is restricted by the maximum track length of about 100 km. The cross-track resolution varies with the maximum footprint that strongly depends on the elevation with an average of 0.2 km (at $E > 15°$) and 3.8 km (at $E < 5°$).

4. Conclusions

A GNSS-R phase retrieval is applied to data recorded during the GEOHALO flight mission. It depicts geoid undulations of the Mediterranean Sea. Some phase residuals resolve changes of the sea surface topography with centimeter precision. The phase retrieval requires a precise path model. Large-scale modeling uses ray tracing. Small-scale modeling accounts for high-rate changes of the aircraft height. Within the described limits of spatial resolution (1–100 km) these tracks can potentially improve the detection of sea surface anomalies such as those induced by mesoscale ocean eddies.

The phase ambiguity limits the retrieval's accuracy. Ambiguity solutions have been proposed for ground-based phase altimetry [*Treuhaft et al.*, 2001; *Belmonte Rivas and Martin-Neira*, 2006; *Beckheinrich et al.*, 2012]. The surface topography, that is important for airborne phase altimetry, adds a new challenge. In this case the integration of other techniques can provide reference for ambiguity solution leading to the following synergies. GNSS-R code retrievals, e.g., [*Carreno-Luengo et al.*, 2013], could assist and benefit from an improved along-track resolution. Current altimeter missions could provide reference at track crossings and benefit from a densified sampling.

Conditions for this phase retrieval are optimal between 10° and 30° of elevation. At elevations below, the phase shows a reduced height sensitivity and a drastically increased footprint size. At elevations above, the ocean roughness drastically reduces the number of continuous phase observations.

Future studies may also use down-looking patch antennas for phase altimetry as they offer a better field of view in azimuth with an acceptable gain in the optimal elevation range. Furthermore, future studies should also focus on polar regions with different roughness conditions of sea ice and snow surfaces. These regions are particularly suitable for GNSS-R exploration as previous studies have indicated [*Beyerle et al.*, 2002; *Cardellach et al.*, 2004; *Fabra et al.*, 2011].

Acknowledgments
We would like to thank our partners at DLR and ETH for their support during the GEOHALO mission. The ECMWF is gratefully acknowledged for providing meteorological data. We are also grateful for the provision of GPS ephemerides by R. König and for GNSS reference data provided by BKG, E-GEOS, Politecnico di Torino, Università degli Studi di Napoli e di Perugia.

The Editor thanks two anonymous reviewers for their assistance in evaluating this paper.

References

Ablain, M., J. Dorandeu, P. Le Traon, and A. Sladen (2006), High resolution altimetry reveals new characteristics of the December 2004 Indian Ocean tsunami, *Geophys. Res. Lett.*, *33*, L21602, doi:10.1029/2006GL027533.

Andersen, O. B., and P. Knudsen (2009), DNSC08 mean sea surface and mean dynamic topography models, *J. Geophys. Res.*, *114*, C11001, doi:10.1029/2008JC005179.

Beckheinrich, J., G. Beyerle, S. Schön, H. Apel, M. Semmling, and J. Wickert (2012), WISDOM: GNSS-R based flood monitoring, *Reflectometry Using GNSS and Other Signals of Opportunity (GNSS+R), 2012 Workshop on,* IEEE, doi:10.1109/GNSSR.2012.6408257.

Beckmann, P., and A. Spizzichino (1987), *The Scattering of Electromagnetic Waves from Rough Surfaces*, International Series of Monographs on Electromagnetic Waves, vol. 4, Pergamon Press, Artech House, Inc., Nordwood, MA, reprint. Originally published: Oxford [Oxfordshire], 1963, New York.

Belmonte Rivas, M., and M. Martin-Neira (2006), Coherent GPS reflections from the sea surface, *IEEE Geosci. Remote Sens. Lett.*, *3*(1), 28–31.
Beyerle, G., K. Hocke, J. Wickert, T. Schmidt, C. Marquardt, and C. Reigber (2002), GPS radio occultations with CHAMP: A radio holographic analysis of GPS signal propagation in the troposphere and surface reflections, *J. Geophys. Res.*, *107*(D24), 4802–4815, doi:10.1029/2001JD001402.
Blewitt, G. (1989), Carrier phase ambiguity resolution for the global positioning system applied to geodetic baselines up to 2000 km, *J. Geophys. Res.*, *94*(B8), 10,187–10,203.
Bosch, W., R. Savcenko, D. Dettmering, and C. Schwatke (2012), A two-decade time series of eddy-resolving dynamic ocean topography (iDOT), in *Proceedings of 20 Years of Progress in Radar Altimetry, Sept. 2012*, Venice, Italy, ESA SP-710 [CD-ROM], ISBN 978-92-9221-274-2, ESA/ESTEC, 2013.
Cardellach, E., C. O. Ao, M. de la Torre Juárez, and G. A. Hajj (2004), Carrier phase delay altimetry with GPS-reflection/occultation interferometry from low earth orbiters, *Geophys. Res. Lett.*, *31*, L10402, doi:10.1029/2004GL019775.
Carreno-Luengo, H., H. Park, A. Camps, F. Fabra, and A. Rius (2013), GNSS-R derived centimetric sea topography: An airborne experiment demonstration, *IEEE Sel. Top. Appl. Earth Obs. Remote Sens.*, *6*(3), 1468–1478, doi:10.1109/JSTARS.2013.2257990.
Fabra, F., E. Cardellach, A. Rius, S. Ribó, S. Oliveras, M. Belmonte, M. Semmling, and S. D'Addio (2011), Phase altimetry with dual polarization GNSS-R over sea ice, *IEEE Trans. Geosci. Remote Sens.*, *50*(6), 2112–2121, doi:10.1109/TGRS.2011.2172797.
Förste, C., et al. (2011), EIGEN-6—A new combined global gravity field model including GOCE data from the collaboration of GFZ-Potsdam and GRGS-Toulouse, in *Geophys. Res. Abstr.*, vol. 13, EGU2011-3242-2, EGU General Assembly.
Fu, L. L., D. B. Chelton, P.-Y. Le Traon, and R. Morrow (2010), Eddy dynamics from satellite altimetry, *Oceanography*, *23*(4), 14–25.
Ghiglia, D. C., and M. D. Pritt (1998), *Two-Dimensional Phase Unwrapping: Theory, Algorithms, and Software*, Wiley VCH, New York.
Heyde, I., F. Barthelmes, and M. Scheinert (2013), First results of the aerogravity measurements during the geoscientific flight mission GEOHALO over Italy and the adjacent Mediterranean, in *Geophys. Res. Abstr.*, vol. 15.
Lowe, S. T., C. Zuffada, Y. Chao, P. Kroger, L. E. Young, and J. L. LaBrecque (2002), 5-cm-precision aircraft ocean altimetry using GPS reflections, *Geophys. Res. Lett.*, *29*(10), 1375–1378, doi:10.1029/2002GL014759.
Martin-Neira, M. (1993), A passive reflectometry and interferometry system (PARIS): Application to ocean altimetry, *ESA Journal*, *17*, 331–355, Radio-Frequency Division, ESTEC, Noordwijk, The Netherlands.
Misra, P., and P. Enge (2001), *Global Positioning System - Signals, Measurements, and Performance*, Ganga-Jamuna Press, Lincoln, Mass.
Pavlis, N. K., S. A. Holmes, S. C. Kenyon, and J. K. Factor (2012), The development and evaluation of the Earth gravitational model 2008 (EGM2008), *J. Geophys. Res.*, *117*, B04406, doi:10.1029/2011JB008916.
Rius, A., E. Cardellach, and M. Martin-Neira (2010), Altimetric analysis of the sea surface GPS reflected signals, *IEEE Trans. Geosci. Remote Sens.*, *48*, 2119–2127.
Ruffini, G., F. Soulat, M. Caparrini, O. Germain, and M. Martín-Neira (2004), The eddy experiment: Accurate GNSS-R ocean altimetry from low altitude aircraft, *Geophys. Res. Lett.*, *31*, L12306, doi:10.1029/2004GL019994.
Scheinert, M. (2013), The geodetic-geophysical flight mission GEOHALO to acquire measurements of the gravity and magnetic fields, of GNSS remote sensing and of laser altimetry over the Mediterranean, in *Geophys. Res. Abstr.*, vol. 15.
Schlager, H., S. Gemsa, and A. Schütz (2013), To the Antarctic and back-in ten days, *DLR Magazine*, *(136/137)*, 50–53, Deutsches Zentrum für Luft- und Raumfahrt e. V. German Aerospace Center (DLR), Cologne, Germany.
Semmling, A. M., T. Schmidt, J. Wickert, S. Schön, F. Fabra, E. Cardellach, and A. Rius (2012), On the retrieval of the specular reflection in GNSS carrier observations for ocean altimetry, *Radio Sci.*, *47*, RS6007, doi:10.1029/2012RS005007.
Semmling, A. M., J. Wickert, S. Schön, R. Stosius, T. Gerber, M. Markgraf, M. Ge, and G. Beyerle (2013), A zeppelin experiment to study airborne altimetry using specular Global Navigation Satellite System reflections, *Radio Sci.*, *48*, 427–440, doi:10.1002/rds.20049.
Semmling, M. (2012), *Altimetric Monitoring of Disko Bay Using Interferometric GNSS Observations on L1 and L2*, Scientific Technical Report STR12/04, GFZ German Research Centre for Geosciences, Helmholtz Centre Potsdam.
Smyrnaios, M., S. Schön, and M. Liso Nicolás (2013), *Geodetic Sciences - Observations, Modeling and Applications*, Multipath Propagation, Characterization and Modeling in GNSS. pp. 99–125, intech.
Treuhaft, R. N., S. T. Lowe, C. Zuffada, and Y. Chao (2001), 2-cm GPS altimetry over crater lake, *Geophys. Res. Lett*, *22*(23), 4343–4346.
Wang, Q., T. Xu, and G. Xu (2010), *HALO GPS Software User Manual*, Scientific Technical Report STR10/11, GFZ German Research Centre for Geosciences, Helmholtz Centre Potsdam.